

# Analysis note for $K_S^0$ , $\Lambda$ , $\bar{\Lambda}$ , $\Xi^-$ , $\Xi^+$ production in Au+Au collisions at $\sqrt{s_{NN}} = 7.7, 11.5, 19.6, 27, \text{ and } 39 \text{ GeV}$

Xianglei Zhu  
Tsinghua University

April 12, 2017

## Abstract

In this note, we present the details of the analysis for  $K_S^0$ ,  $\Lambda$ ,  $\bar{\Lambda}$ ,  $\Xi^-$ ,  $\Xi^+$  production in Au+Au collisions at  $\sqrt{s_{NN}} = 7.7, 11.5, 19.6, 27, \text{ and } 39 \text{ GeV}$ . The experimental data was taken by STAR in year 2010 for 7.7, 11.5 and 39 GeV, and in year 2011 for 19.6 and 27 GeV. We present the details of the dataset that was used in this analysis first. Then we describe the analysis cuts used for strange hadron reconstruction, the invariant mass distributions for all strange hadrons, the signal extraction methods, and thereafter the uncorrected strange hadron  $p_T$  spectra at mid-rapidity ( $|y| < 0.5$ ) for all energies and centralities. Then the details about the Monte Carlo embedding data samples and the reconstruction efficiencies of various strange hadrons for all energies and centralities will be presented. After that, the corrected  $p_T$  spectra for all strange hadron species at all centralities and energies are presented. Finally, we present the details of systematic uncertainty estimation for  $p_T$  spectra and the integrated yields ( $dN/dy$ ) of various strange hadrons.

## 1 Dataset

The experimental data was taken by STAR in year 2010 (RHIC Run10) for 7.7, 11.5 and 39 GeV, and in year 2011 (Run11) for 19.6 and 27 GeV. The minimum bias trigger at all five energies was defined by the signal coincidence of the Zero-Degree Calorimeters (ZDC), Vertex Position Detectors (VPD), and/or Beam-Beam Counters (BBC). However, at the lowest beam energies, most of the triggered events are “fixed-target” background, which are the Au nuclei from the beam with large emittance hitting on the nuclei at rest in beam pipe. The background can be removed by requiring that the primary vertex (PV) of an event was within a radius  $r$  of less than 2 cm and much less than that of the beam pipe (3.95 cm). The primary vertex position in beam direction (or  $z$ -direction) was limited to the values listed in Table 1. These values were selected according to the offline  $z$ -vertex trigger conditions which were different for different energies, see Fig. 1 (left) for the  $z$ -vertex distribution at each collision energy. It was further required that at least two tracks from the primary vertex were matched to the cells of the barrel time-of-flight detector in order to remove the pile-up events. Finally, events from bad runs were removed according to an extensive quality assurance of the events, for details, see Ref. [1]. The accepted number of minimum bias events for each of the five energies are also listed in Table 1.

Table 1: The data-taking year, data production tag, trigger ID’s,  $z$ -vertex ranges, and the total number of minimum-bias (MB) events used for different collision energies.

$\sqrt{s_{NN}}$ (GeV)	Year	Production tag	Trigger ID	$z$ -vertex range (cm)	MB events ( $10^6$ )
7.7	2010	P10ih	290001,290004	[-70,70]	4.4
11.5	2010	P10ih	310014,310004	[-50,50]	12.0
19.6	2011	P11id	340001,340011,340021	[-70,70]	36.3
27	2011	P11id	360001	[-70,70]	72.8
39	2010	P10ik	280001	[-40,40]	134.4

The centrality selection of the events was chosen to be 0–80% of the total reaction cross section due to trigger inefficiencies for most peripheral events. The centrality definition was based on uncorrected multiplicity distribution (see the right panel in Fig. 1) and the Glauber Monte Carlo simulation [2], whose details can be found in Refs. [1, 3]. With the comparison of the Glauber simulation and the measured multiplicity distribution at each energy, it is possible to determine for each centrality class

the average number of participant nucleons  $\langle N_{\text{part}} \rangle$  and the average number of nucleon-nucleon binary collisions  $\langle N_{\text{bin}} \rangle$  at this energy. The ‘**StRefMultCorr**’ package (ver. 1.8) [3] was used for centrality determination and bad runs rejection in this analysis.

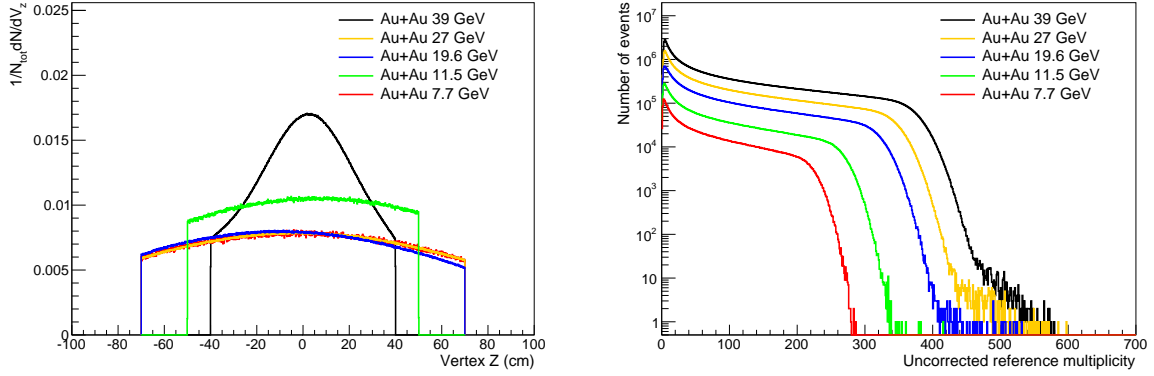


Figure 1: (left) Normalized distribution of event primary vertex  $z$  coordinate at different BES energies. (right) Distribution of the uncorrected reference multiplicity measured by TPC at different BES energies.

## 2 Analysis cuts

The strange hadrons,  $K_S^0$ ,  $\Lambda(\bar{\Lambda})$  and  $\Xi^-(\bar{\Xi}^+)$  have short life-times, and decay into a pair of charged particles or into one charge particle plus a  $\Lambda(\bar{\Lambda})$ . All of them can be reconstructed using the invariant mass technique. The corresponding decay channels and branching ratios are,

$$K_S^0 \rightarrow \pi^+ + \pi^-, \quad 69.20\%$$

$$\Lambda(\bar{\Lambda}) \rightarrow p(\bar{p}) + \pi^-(\pi^+), \quad 63.9\%$$

$$\Xi^-(\bar{\Xi}^+) \rightarrow \Lambda(\bar{\Lambda}) + \pi^-(\pi^+), \quad 99.887\%$$

The mean specific energy loss,  $\langle dE/dx \rangle$ , measured by the TPC was used for identification of the charged daughter particles,  $\pi^\pm$ ,  $K^\pm$  and  $p(\bar{p})$  [5]. Despite the random nature of the measured  $\langle dE/dx \rangle$  for a certain track due to the limited number of hit points measured by TPC, the center values of the measured  $\langle dE/dx \rangle$  for a certain particle species as a function of  $p_T$  can be well described by the Bichsel function [6]. Hence a normalized  $\langle dE/dx \rangle$ ,  $n\sigma_{\text{particle}}$ , was used in particle identification. It is defined by

$$n\sigma_{\text{particle}} = \frac{1}{\sigma_{\text{particle}}} \log \frac{\langle dE/dx \rangle_{\text{measured}}}{\langle dE/dx \rangle_{\text{particle}}^{\text{Bichsel}}},$$

where  $\langle dE/dx \rangle_{\text{particle}}^{\text{Bichsel}}$  is the expected  $\langle dE/dx \rangle$  from Bichsel function for a certain particle species at a given  $p_T$ , and  $\sigma_{\text{particle}}$  is the  $\langle dE/dx \rangle$  resolution of TPC for the same particle species at the same  $p_T$ . The  $n\sigma_{\text{particle}}$  distribution is nearly Gaussian at a given momentum and is properly calibrated to be centered at zero for each particle species with a width of unity. By default, a loose cut of  $|n\sigma_{\text{particle}}| < 4.0$  was used to select all the corresponding charged daughter particles for the reconstruction of  $K_S^0$ ,  $\Lambda(\bar{\Lambda})$  and  $\Xi^-(\bar{\Xi}^+)$ . At 27 GeV, the  $n\sigma_{\text{particle}}$  values have been multiplied by a factor of 2 to correct the issue of  $n\sigma_{\text{particle}}$  calculation in the 27 GeV data production. In order to improve the average momentum and energy loss resolution, the charged daughter particle tracks were required to consist of at least 16 TPC hit points for the reconstruction of  $K_S^0$ ,  $\Lambda(\bar{\Lambda})$ , and  $\Xi^-(\bar{\Xi}^+)$ .

Due to the large number of final state particles in Au+Au collisions, there are significant amount of combinatorial background in the invariant mass distributions of all strange hadrons. The weakly decayed strange hadrons,  $K_S^0$ ,  $\Lambda(\bar{\Lambda})$ ,  $\Xi^-(\bar{\Xi}^+)$ , have a typical life-time of  $c\tau \sim 2 - 7$  cm. Their decay topology can be well reconstructed with their daughter particle tracks measured by TPC with a precision of  $\sim 1$  mm. Figure 2 shows  $V^0$  ( $K_S^0$  and  $\Lambda$ ) and  $\Xi$  decay topological structures. The private  $V^0$  and  $\Xi$  decay vertex finders (called ‘**StV0Maker**’ and ‘**StXiMaker**’, included in the analysis code package) were used

to extrapolate the measured TPC tracks towards the main Au+Au collision vertex, hence to find the  $V^0$  or  $\Xi$  decay vertex, where the extrapolated daughter tracks are closest to each other. Therefore, certain set of cuts can be applied to the topological geometry variables in order to significantly reduce the combinatorial background. Such variables include the distance of closest approach (DCA) between the two daughter tracks, the DCA's of the daughter tracks and the reconstructed strange hadron track to the primary vertex, the pointing away cut (the dot product of the relative position vector of  $V^0$  decay vertex to PV and the  $V^0$  momentum vector is required to be larger than 0, i.e.  $(\vec{r}_{V^0} - \vec{r}_{PV}) \cdot \vec{p}_{V^0} > 0$ ) and the decay length of strange hadrons (see their exact definitions in the left panel of Fig. 2). Those cuts were optimized by considering a compromise between reducing combinatorial background and increasing reconstruction efficiency. Table 2 shows the geometrical cuts used for  $K_S^0$ ,  $\Lambda(\bar{\Lambda})$  reconstruction in this analysis. The same cuts were used in the analyses at all BES energies and centralities, except for  $\bar{\Lambda}$  at 7.7 GeV, tighter cuts (shown in Table 2, together with a tighter  $|n\sigma_{\text{particle}}| < 3.8$ ) were used to optimize the significance of the signals, hence to reduce the statistical errors.

For the reconstruction of multi-strange hyperons,  $\Xi^-(\Xi^+)$ , the  $\Lambda$  candidates reconstructed with  $p$  and  $\pi$  daughter tracks are further combined with the bachelor charged particle track,  $\pi^\pm$ , for the  $\Xi$  reconstruction. In order to reduce combinatorial background, the  $\Lambda$  candidates were required to be inside the invariant mass window of  $1.115683 \pm 0.012$  GeV/ $c^2$  for  $\Xi$  reconstruction. The decay topology of multi-strange hyperons are more complicated compared to those of  $V^0$  particles, hence more topological geometrical cuts were used in the hyperon reconstructions (see the right panel of Fig. 2). Table 3 shows the default geometrical cuts for  $\Xi$  reconstruction in this analysis. The same cuts were used in the analyses at all centralities, but slightly tighter cuts were used for 11.5 and 7.7 GeV, as shown in Table 2, in order to optimize the significance of the signals, hence to reduce the statistical errors. At 11.5 and 7.7 GeV, a tighter  $|n\sigma_{\text{particle}}| < 3.6$  and slightly narrower  $\Lambda$  invariant mass window of  $1.115683 \pm 0.010$  GeV/ $c^2$  were used as well.

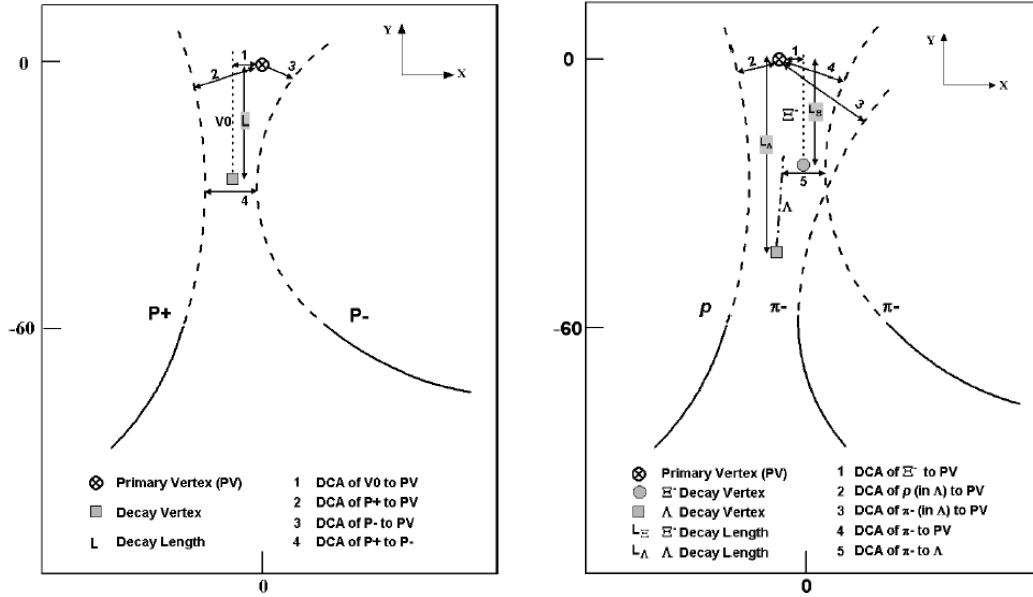


Figure 2: (left)  $V^0$  ( $K_S^0$  or  $\Lambda$ ) and (right)  $\Xi$  decay topological structure seen in the transverse plane, taken from Hai Jiang's thesis [7]. The solid lines are inside TPC fiducial volume and detectable by the TPC anode sectors, which are 600.00 mm away from the detector center. The dashed lines are the extrapolations of solid lines inside the TPC inner field cage or reconstructed  $V^0$  and  $\Xi$ . The topological cut variables are listed in the figure.

With those cuts, there are still background left under the mass peak of each hadrons. The random combinatorial background were estimated with the rotation method for  $K_S^0$ ,  $\Lambda$  and  $\Xi$ . In the rotation method, one daughter particle track was picked, for example,  $\pi^-$  in case of  $K_S^0$  reconstruction. Then both the 2-dim vectors (in the transverse plane) of this track's starting point position (with respect to PV) and its momentum were rotated by an angle of  $\pi$ . The rotated track was used in the strange hadron reconstruction. The track rotation was supposed to break all the possible correlations between the daughter particles and mimic the random combination contribution in strange hadron reconstructions.

Table 2: Topological cuts used for the  $V^0$  particles,  $K_S^0$  and  $\Lambda(\bar{\Lambda})$ , reconstruction.

Cut	$K_S^0$	$\Lambda$ and $\bar{\Lambda}$
DCA of $V^0$ to primary vertex	$< 0.8$ cm	$< 0.8$ cm
DCA of $V^0$ -daughters to primary vertex	$> 0.7$ cm	$> 0.3$ cm ( $p$ ), $> 1.0$ cm ( $\pi$ ) $\bar{\Lambda}$ at 7.7 GeV: $> 0.5$ cm ( $p$ ), $> 1.5$ cm ( $\pi$ )
DCA between $V^0$ -daughters	$< 0.8$ cm	$< 0.8$ cm
Radial decay length	$> 2.5$ cm	$> 3$ cm $\bar{\Lambda}$ at 7.7 GeV: $> 4$ cm
Pointing away	$(\vec{r}_{V^0} - \vec{r}_{PV}) \cdot \vec{p}_{V^0} > 0$	$(\vec{r}_{V^0} - \vec{r}_{PV}) \cdot \vec{p}_{V^0} > 0$

Table 3: Topological cuts used for  $\Xi^-(\Xi^+)$  reconstruction.

Cut	$\Xi^-$ and $\Xi^+$
DCA of $\Xi$ to primary vertex	$< 0.8$ cm
DCA of bachelor to primary vertex	$> 0.8$ cm
DCA of $V^0$ to primary vertex	$[0.2, 5.0]$ cm
DCA of $V^0$ -daughter $p$ to primary vertex	$> 0.5$ cm
DCA of $V^0$ -daughter $\pi$ to primary vertex	$> 1.0$ cm
	11.5 and 7.7 GeV: $> 1.5$ cm
DCA between $V^0$ and bachelor	$< 0.8$ cm
DCA between $V^0$ -daughters	$< 0.8$ cm
$\Xi$ decay length	$> 3.4$ cm
	11.5 and 7.7 GeV: $> 4.0$ cm
$V^0$ decay length	$> 5.0$ cm
Pointing away	$(\vec{r}_{V^0} - \vec{r}_{PV}) \cdot \vec{p}_{V^0} > 0,$ $(\vec{r}_{V^0} - \vec{r}_{\Xi}) \cdot \vec{p}_{V^0} > 0,$ $(\vec{r}_{\Xi} - \vec{r}_{PV}) \cdot \vec{p}_{\Xi} > 0$
Collinear angle cut	$(\vec{r}_{\Xi} - \vec{r}_{PV}) \times \vec{p}_{\Xi} /  \vec{r}_{\Xi} - \vec{r}_{PV}   \vec{p}_{\Xi}  < 0.2$ 11.5 and 7.7 GeV: $(\vec{r}_{\Xi} - \vec{r}_{PV}) \times \vec{p}_{\Xi} /  \vec{r}_{\Xi} - \vec{r}_{PV}   \vec{p}_{\Xi}  < 0.12$

Besides the combinatorial background, there are also residual background for each particle. The origin of the residual background is due to particle mis-identification. For example, the proton from a  $\Lambda$  decay can be mis-identified as a  $\pi^+$ , combined with the  $\Lambda$ 's  $\pi^-$  daughter, will contribute to the residual background in  $K_S^0$  reconstruction. In  $\Xi$  reconstruction, a real  $\Lambda$ 's proton daughter can be combined with another random pion to form a fake  $\Lambda$  candidate, then the fake  $\Lambda$  is combined with the real  $\Lambda$ 's pion daughter (as the bachelor pion) to form a fake  $\Xi$ . In order to remove those kinds of residual background, veto cuts were introduced. In  $K_S^0$  reconstruction, the  $\pi^+$  and  $\pi^-$  daughters of a  $K_S^0$  candidate were assumed to be the  $p$  and  $\bar{p}$  daughters of a  $\Lambda$  and a  $\bar{\Lambda}$  to re-calculate the invariant masses separately. If they fall inside the invariant mass window of  $[1.1057, 1.165]$  GeV/ $c^2$ , this  $K_S^0$  candidate will be rejected. For  $\Xi$  reconstruction, the proton daughter will be combined with the pion bachelor to calculate the invariant mass. If it falls inside the  $\Lambda$  invariant mass window of  $1.115683 \pm 0.010$  GeV/ $c^2$ , this  $\Xi$  candidate will be rejected. There are also minor residual background in  $\Lambda$  invariant mass distribution due to the mid-identification of  $K_S^0$  daughters. However, the veto of this residual background will cost significant drop in  $\Lambda$  reconstruction efficiency due to the large width of  $K_S^0$  invariant mass peak, hence there are no veto cuts for  $\Lambda$ . The veto cuts for  $K_S^0$  and  $\Xi$  are applied both in signal reconstruction and in rotational background reconstruction.

### 3 Signal extraction

The invariant mass distributions of  $K_S^0$ ,  $\Lambda$ ,  $\bar{\Lambda}$ ,  $\Xi^-$  and  $\Xi^+$  were then subtracted with those from the corresponding rotational background, except for  $\bar{\Lambda}$  at 7.7 GeV. A double gaussian plus polynomial fitting

to the resulting invariant mass distribution around the signal peaks was used to determine the signal peak width as well as the shape of the remaining residual background. The total number of signal candidates were then obtained by subtracting the total counts of candidates inside the signal peak with that of background inside the peak, while the latter was estimated either by the polynomial fitting functions or by the side-band method.

Figure 3 shows the  $K_S^0$  invariant mass distribution after rotational background subtraction and the fitting results at one  $p_T$  bin in most central Au+Au collisions at 39 GeV. The fitting failed at higher  $p_T$  bins due to limited statistics, the side-band method was used to estimated the background inside the signal peak. The signal peak width (and the side-bands regions) were determined by the fitting where it is applicable. The resulting width increases toward higher  $p_T$ , this trend is consistent with the  $K_S^0$  embedding simulation results. Therefore, the signal peak width at higher  $p_T$  bins were determined by considering both the low  $p_T$  fitting results and the trend from embedding simulation. For  $K_S^0$  signal extraction in all  $p_T$  bins, at all centrality and energies, please refer to Ref. [8].

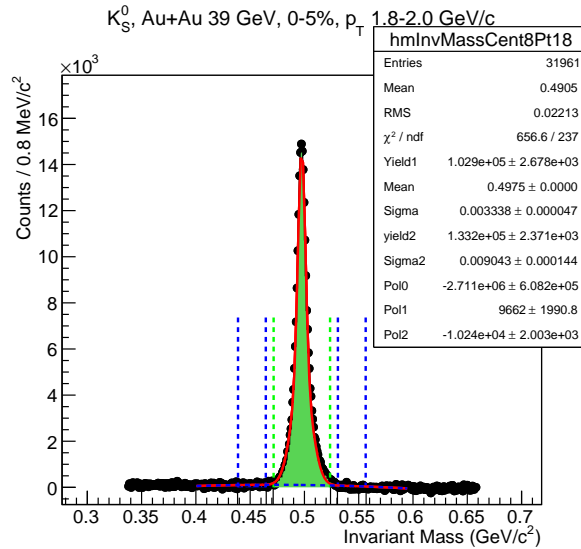


Figure 3:  $K_S^0$  invariant mass distributions at mid-rapidity ( $|y| < 0.5$ ), for the  $p_T$  bin of  $[1.8, 2.0]$  GeV/c, from the most central (0-5%) Au+Au collisions at  $\sqrt{s_{NN}} = 39$  GeV. The combinatorial background, which were estimated with rotational method, has been subtracted. The distribution was fitted with double gaussian (for signal peak) plus polynomial functions (for background), shown as the red line. The horizontal blue dashed line represents the background. The vertical green dashed lines and green shaded area show the signal peak region, while the blue lines and shaded areas define the side-band regions both sides of the peak.

Figure 4 shows the  $\Lambda$  and  $\bar{\Lambda}$  invariant mass distribution after rotational background subtraction and the fitting results at one  $p_T$  bin in most central Au+Au collisions at 39 GeV. Since the shape of residual background is slightly asymmetric around the peak, the fitting method was used for most  $p_T$  bins, except for those with very low statistics where the side-band methods were used. At higher  $p_T$  bins, where the statistics is relatively lower, a single gaussian plus polynomials fitting was used to determine the residual background shape. The signal peak width at higher  $p_T$  bins were determined by considering both the low  $p_T$  fitting results and the trend from embedding simulation. For  $\Lambda$  and  $\bar{\Lambda}$  signal extraction in all  $p_T$  bins, at all centrality and energies, please refer to Ref. [9]. For  $\bar{\Lambda}$  at 7.7 GeV, the invariant mass distributions were fitted directly without subtracting the rotational background, in order to reduce the statistical errors due to low statistics there.

Figure 5 shows the  $\Xi^-$  and  $\Xi^+$  invariant mass distribution after rotational background subtraction and the double gaussian plus polynomial fitting results at one  $p_T$  bin in most central Au+Au collisions at 39 GeV. The fitting failed at higher  $p_T$  bins due to limited statistics, the side-band method was used to estimated the background inside the signal peak. The signal peak width and the side-bands regions were determined by the fitting where it is applicable. While at higher  $p_T$  bins, the peak width and the side-band regions were determined by considering both the low  $p_T$  fitting results and the trend from

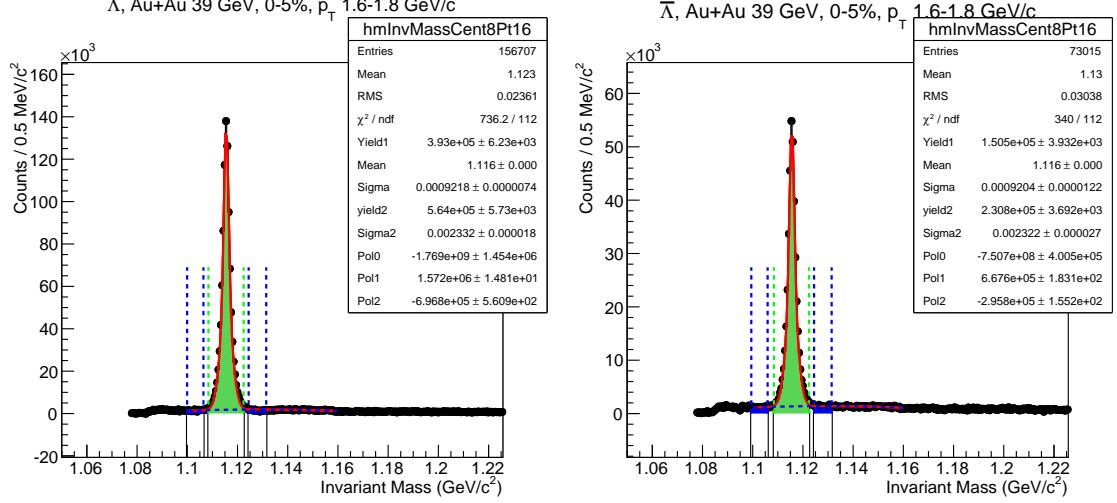


Figure 4:  $\Lambda$  (left) and  $\bar{\Lambda}$  (right) invariant mass distributions at mid-rapidity ( $|y| < 0.5$ ), for the  $p_T$  bin of  $[1.6, 1.8]$  GeV/c, from the most central (0-5%) Au+Au collisions at  $\sqrt{s_{NN}} = 39$  GeV. The combinatorial background, which were estimated with rotational method, has been subtracted. The fitting method and the lines are depicted more in Fig. 3.

embedding simulation. For  $\Xi^-$  and  $\Xi^+$  signal extraction in all  $p_T$  bins, at all centrality and energies, please refer to Ref. [10].

## 4 Uncorrected $p_T$ spectra

With the method described in Sec. 3, the numbers of signal candidates  $N$  at mid-rapidity ( $|y| < 0.5$ ) can be obtained for all  $p_T$  bins at different collision centralities and energies. Figures 6, 7, 8, 9 and 10 show the resulting uncorrected  $p_T$  spectra of  $K_S^0$ ,  $\Lambda$ ,  $\bar{\Lambda}$ ,  $\Xi^-$  and  $\Xi^+$ , at mid-rapidity, for different collision centralities and energies.

## 5 Reconstruction efficiency

The STAR TPC tracking efficiency and hence the strange hadrons reconstruction efficiency significantly depend on the final state particle multiplicity which ranges from a few in peripheral collisions to about a thousand in most central collisions. In STAR, the acceptance and reconstruction efficiencies for each analyzed particles were calculated using an embedding technique, in which the simulated Monte Carlo (MC) particles sampled in a given kinematic range were embedded into real events where the efficiency was studied. The number of embeded particles per event is about 5% of the measured charged particle multiplicities of this event, and they are all placed in the primary vertex of this event. The subsequent strange hadrons propagation and decay, the charged daughter particles propagation in STAR, and the TPC detector response to the charged daughter particles were simulated with the GEANT package and the STAR TPC response simulator (TpcRS). The simulated electronics signals were mixed with those from the real event, and then processed with the STAR tracking, event reconstruction, and the strange hadron reconstruction software packages. The acceptance and reconstruction efficiency were obtained by dividing the number of reconstructed MC strange hadrons by that of input MC ones in a certain kinematic range.

Practiacally, only a small subset ( $\sim 50$  K events) of the real data events were used for embedding simulation. It is required that the subset can sample as many runs as possible to cover different run conditions during the data taking, therefore they should have similar vertex- $z$  and reference multiplicity distribution as the full set of the real data events. The same event cuts were applied to the embedding events during the analysis. For the kinematic variables of input MC strange particles, their rapidity distribution is flat within  $|y| < y_{max}$ , with  $y_{max}$  larger than 0.5. The  $p_T$  distribution is sampled in two different ways: one is flat within  $[0, p_{Tmax}]$ , with  $p_{Tmax}$  of about 2 GeV/c larger than the max measurable

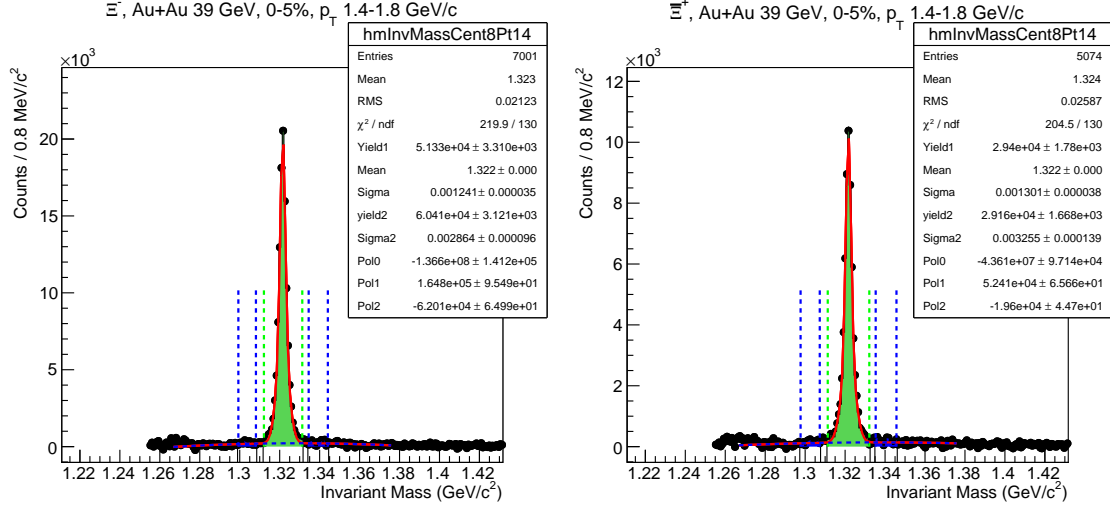


Figure 5:  $\Xi^-$  (left) and  $\Xi^+$  (right) invariant mass distributions at mid-rapidity ( $|y| < 0.5$ ), for the  $p_T$  bin of  $[1.4, 1.8]$  GeV/c, from the most central (0-5%) Au+Au collisions at  $\sqrt{s_{NN}} = 39$  GeV. The combinatorial background, which were estimated with rotational method, has been subtracted. The fitting method and the lines are depicted more in Fig. 3.

$p_T$  in real data; another way is exponential distribution,  $dN/dp_T \propto p_T \exp(-p_T/T)$ , with  $T = 350$  MeV. The reconstruction efficiency of strange particle has a generally increasing trend with increasing  $p_T$ , from a few percent at the lowest  $p_T$  bin to 40-50% at the largest  $p_T$  bin. As a result, the number of reconstructed MC particles at lower  $p_T$  are much smaller than that at high  $p_T$  in the case of flat input MC  $p_T$ , therefore the efficiency has much larger statistical errors at lower  $p_T$  bins, on the contrary to the fact that the measured uncorrected  $p_T$  spectra has much smaller statistical errors at lower  $p_T$  bins (seen in Sec. 4). The exponential  $p_T$  sample increases the statistics at lower  $p_T$  bins significantly, hence can help reduce the statistical errors there. This is important for the yield ' $dN/dy$ ' measurement, where the lower  $p_T$  bins have major contributions. Quality assurance checks have been performed for all of the embedding samples at different energies. Almost all of the cut variables distribution from embedding MC data have been compared to the corresponding real data. Ref. [11] show the 'Base QA' provided by the STAR embedding team and our 'PWG QA' comparison figures at 39 GeV for  $K_S^0$ ,  $\Lambda$ , and  $\Xi^-$  embedding samples.

In this analysis, the  $p_T$  binning used in efficiency calculation is exactly the same as that in uncorrected spectra in Sec. 4. The bin width could be as large as  $\sim 1$  GeV/c at very high  $p_T$ , where the particle  $p_T$  spectra decrease exponentially with increasing  $p_T$ . Therefore, each MC particle had to be assigned a weight according to the real  $p_T$  distribution, which was obtained from a fit to the particle efficiency-corrected  $p_T$  spectra at mid-rapidity. The efficiencies at each  $p_T$  bin were calculated separately with flat  $p_T$  samples and exponential  $p_T$  samples respectively. It has been verified that the two efficiencies are consistent with each other within uncertainties. The final efficiency are weighted sum of both efficiencies in order to further reduce statistical uncertainties.

The calculated efficiencies at mid-rapidity ( $|y| < 0.5$ ) for different strange particles in peripheral (60-80%) and most central (0-5%) Au+Au collisions at 39 GeV are shown as a function of  $p_T$  in Fig. 11. Comparing the efficiencies in those two centralities, a significant drop at low  $p_T$  towards central collisions can be observed for all particles. Figure 12 shows the corresponding efficiencies at 7.7 GeV. For the efficiencies in other centrality bins and collision energies, please refer to Ref. [12].

## 6 Corrected $p_T$ spectra for $K_S^0$ , $\Xi^-$ and $\Xi^+$

Figures 13, 14 and 15 show the transverse momentum distribution of  $K_S^0$ ,  $\Xi^-$  and  $\Xi^+$  particles with  $|y| < 0.5$  in different collision centralities from Au+Au collisions at  $\sqrt{s_{NN}} = 7.7, 11.5, 19.6, 27$  and 39 GeV. The spectra have been corrected for the geometrical acceptance and reconstruction efficiency, which is presented in Sec. 5. For better visualization, the spectra are scaled by factors of 10 from central to

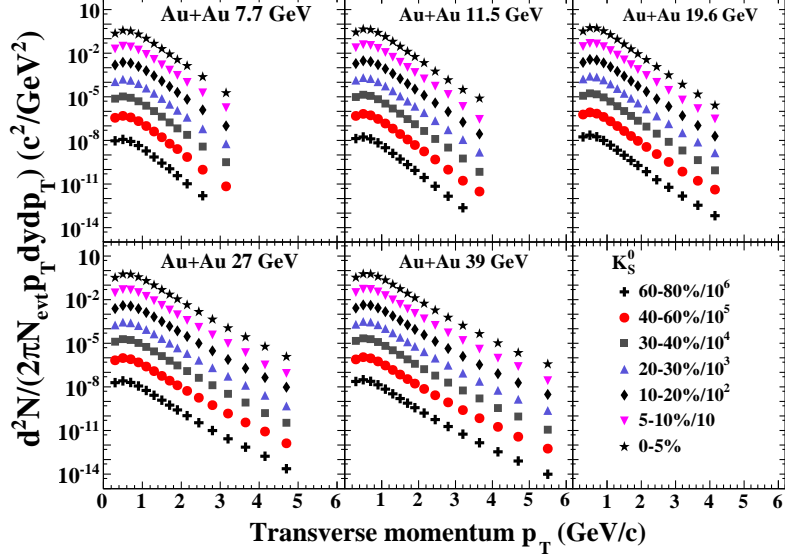


Figure 6: The uncorrected transverse momentum spectra of  $K_S^0$  at mid-rapidity ( $|y| < 0.5$ ) from Au+Au collisions at different centralities and energies ( $\sqrt{s_{NN}} = 7.7 - 39$  GeV). The data points are scaled by factors of 10 from central to peripheral for clarity.

peripheral. The red vertical shaded bands represent systematic errors, which will be described in Sec. 9.

## 7 Feed-down correction for $\Lambda$ and $\bar{\Lambda}$

The reconstructed  $\Lambda$ 's with the cuts listed in Table 2 contains both the prompt  $\Lambda$ 's originating from the primary vertex and those from the weak decays of  $\Xi$ ,  $\Xi^0$  and  $\Omega$  hyperons. Naturally, the  $\Lambda$ 's from secondary vertices have different distributions in topological cut variables compared to prompt  $\Lambda$ 's, for example, the DCA of  $V^0$  to primary vertex. As shown in Table 2, a tighter cut on the distance of closest approach between the reconstructed  $\Lambda$  candidate and the primary vertex was used to reduce the secondary contributions. However, some fractions of the secondary  $\Lambda$ 's still passed this criteria, especially in the high  $p_T$  regions. Hence it is mandatory to subtract their contributions to the reconstructed  $\Lambda$ 's, before applying the prompt  $\Lambda$ 's acceptance and efficiency corrections described in Sec. 5.

The feed-down contributions in the reconstructed  $\Lambda$  sample were evaluated with the helps of the  $\Xi$  and  $\Xi^0$  MC embedding data. These samples were produced with flat MC input  $p_T$  and  $y$  distributions, covering the measurable  $\Lambda$  kinematic ranges. Each MC  $\Xi$  particle, and hence its daughter  $\Lambda$ , was assigned a weight according to the measured  $\Xi$   $p_T$  spectra shape. The  $\Xi$   $p_T$  spectra shape was obtained from a Boltzmann function fitting to the measured  $\Xi$   $p_T$  spectra, shown in Fig. 14 or 15. Let  $N_\Xi$  to be the total weight for all  $\Xi$  within  $|y| < 0.5$ . And let  $N_{\Lambda \leftarrow \Xi}^i$  to be the total weight for those reconstructed  $\Lambda$ 's within the  $i$ -th  $\Lambda$   $p_T$  bin and  $|y| < 0.5$ , with the cuts listed in Table 2. Then the feed down contribution to the uncorrected signal counts in the  $i$ -th  $p_T$  bin can be written as

$$N_{\Lambda,FD}^i = N_{events} \left( \frac{N_{\Lambda \leftarrow \Xi}^i}{N_\Xi} \frac{dN}{dy} \Big|_{\Xi, y=0} \Delta y Br(\Xi \rightarrow \Lambda \pi \rightarrow p \pi \pi) + \frac{N_{\Lambda \leftarrow \Xi^0}^i}{N_{\Xi^0}} \frac{dN}{dy} \Big|_{\Xi^0, y=0} \Delta y Br(\Xi^0 \rightarrow \Lambda \pi \rightarrow p \pi \pi) \right), \quad (1)$$

where  $\Delta y = 1.0$ ,  $Br$  are the corresponding branching ratios (in embedding, only the measured channel of  $\Xi$  and  $\Lambda$  are simulated), the second term is corresponding to the contributions from  $\Xi^0$ , and  $dN/dy$  is the particle yield at mid-rapidity obtained from the integral of  $p_T$  spectra. For  $\Xi^0$ , we assumed that it has the same yield as  $\Xi$  since it can not be measured by STAR, a separate  $\Xi^0$  embedding sample was produced for the  $\Lambda$  feed-down study, since  $\Xi^0$ 's lifetime is much larger than  $\Xi$ , therefore the topological variables distributions are also very different. The transverse momentum distributions of  $\Lambda(\bar{\Lambda})$  from  $\Xi^-(\Xi^+)$  and  $\Xi^0(\bar{\Xi}^0)$  feed-down are shown in Fig. 16(17).

The  $N_{\Lambda,FD}^i$  can be subtracted from the raw  $\Lambda$  yields. The relative contribution of the secondary  $\Lambda$  from  $\Xi$  and  $\Xi^0$  decays was calculated for each  $p_T$  interval in each collision centrality at each collision energy. For Au+Au collisions at 39 GeV, in 0 – 5% most central collisions, the relative feed down contribution



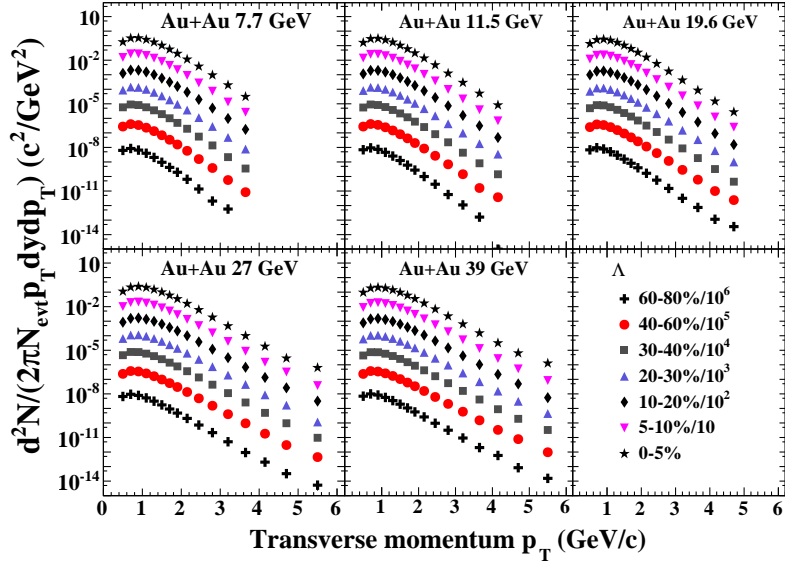


Figure 7: The uncorrected transverse momentum spectra of  $\Lambda$  at mid-rapidity ( $|y| < 0.5$ ) from Au+Au collisions at different centralities and energies ( $\sqrt{s_{NN}} = 7.7 - 39$  GeV). The data points are scaled by factors of 10 from central to peripheral for clarity.

ranges from  $\sim 25\%$  at  $p_T = 0.5$  GeV/c to  $\sim 5\%$  at  $p_T = 5$  GeV/c. The feed down contributions from  $\Omega$  decay was not considered since it is negligible ( $< 1\%$ ) due to the lower yield of  $\Omega$  in the energy range of 7.7 – 39 GeV.

## 8 Corrected $p_T$ spectra for $\Lambda$ and $\bar{\Lambda}$

Figures 18 and 19 show the transverse momentum distribution of  $\Lambda$  and  $\bar{\Lambda}$  particles with  $|y| < 0.5$  in different collision centralities from Au+Au collisions at  $\sqrt{s_{NN}} = 7.7, 11.5, 19.6, 27$  and  $39$  GeV. The spectra have been corrected for the geometrical acceptance and reconstruction efficiency, which is presented in Sec. 5. For better visualization, the spectra are scaled by factors of 10 from central to peripheral. The  $\Lambda(\bar{\Lambda})$  spectra are corrected for the feed-down contribution from the weak decays of  $\Xi$  and  $\Xi^0$  baryons using the measured  $\Xi$  spectra. For more details on feed-down correction, please see Sec. 7. The red vertical shaded bands represent systematic errors, which will be described in Sec. 9.

## 9 Systematic errors on $p_T$ spectra

Many possible sources which can contribute to the systematic uncertainties of the  $p_T$  spectra were evaluated bin-by-bin in this analysis.

In the signal extraction, for  $K_S^0$  and  $\Xi$ , the side-band method and the double Gaussian plus polynomial fitting method were used in the estimation of background in the signal peak region, the difference was taken into account in the systematic uncertainty. The width of the signal peak was first determined by the double Gaussian plus polynomial fitting and then varied to estimate its contribution to systematic error. The shapes of signal peak at high  $p_T$  bins deviated from the symmetric Gaussian shape, the MC simulation data was used to estimate the systematic deviation of the default signal counting method, the deviation seemed to be larger for  $K_S^0$  due to its larger peak width, especially at high  $p_T$ , could reach 5% at 5 GeV/c. For  $\Lambda$ , side-band method can not be used in systematic error estimation due to non-linear background shape, hence the fitting ranges have been changed to account for the possible uncertainty in the background shape, also width of the signal peak was varied to estimate the systematic uncertainty. The deviation of signal peak shape from Gaussian was estimated with MC simulation, the contribution to systematic uncertainty is  $\sim 8\%$  for  $p_T$  at 5 GeV/c. Different sources were assumed to be uncorrelated and hence summed quadratically to obtain the total systematic uncertainty in signal extraction.

The daughter particle identification cuts,  $|n_\sigma|$ , was varied from the default value of 4.0 to 3.6, the change in spectra is negligible. The systematic uncertainties due to tracking were estimated by varying

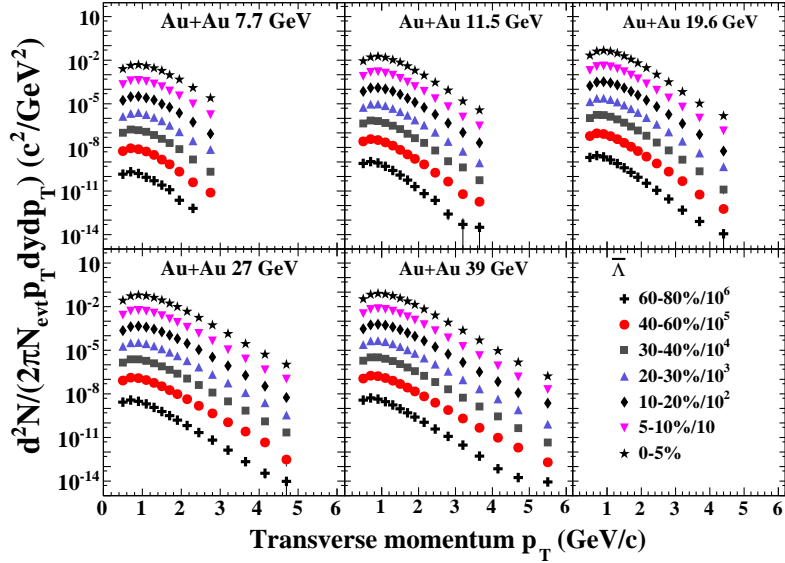


Figure 8: The uncorrected transverse momentum spectra of  $\bar{\Lambda}$  at mid-rapidity ( $|y| < 0.5$ ) from Au+Au collisions at different centralities and energies ( $\sqrt{s_{NN}} = 7.7 - 39$  GeV). The data points are scaled by factors of 10 from central to peripheral for clarity.

the cuts on the minimum number of hit points from the default 15 to 25, the minimum number of hit points used for  $dE/dx$  calculation from 0 to 10, and the minimum ratio of number of hit points to the number of possible hit points from 0.45 to 0.55. The cuts values were changed one at a time, the raw yields and the efficiencies were both re-calculated accordingly to obtain the corrected  $p_T$  spectra. The maximum deviations from the default spectra were accounted for the systematic uncertainties due to this cut. Despite the minor contributions from the later two cuts, the minimum number of daughter hit points, or the tracking, contribute the major systematic uncertainties. The tracking uncertainty are especially larger for tracks with lower  $p_T$  in more central collisions. For  $K_S^0$  and  $\Lambda$  in most central Au+Au collisions at 39 GeV, the uncertainty is  $\sim 6\%$  at  $p_T = 0.5$  GeV/c, while for  $\Xi$ , the value is  $\sim 8\%$  at the same  $p_T$ .

The topological geometric cuts were also varied one after another to study the systematic deviations of  $p_T$  spectra. For example, for  $K_S^0$ , the radial decay length cut value was changed in the range of [2.5, 3.3] cm; the DCA of daughters in [0.55, 0.8] cm; the DCA of  $K_S^0$  in [0.6, 1.2] cm; the DCA between daughters in [0.5, 1.0] cm. The systematic uncertainties from those geometric cuts were generally small compared to the tracking uncertainties. The same method was applied to the systematic error studies for  $\Xi$  and  $\Lambda$  spectra despite that there are more geometrical cuts involved. For this two hyperons, the systematic errors due to those geometric cuts were also small compared to the tracking uncertainties. Alternatively, a detailed comparison was performed between the distributions of the geometrical cut variables from the embedding simulated strange particles and those from the reconstructed strange particles in real data. A good agreement between the MC simulation and the data was achieved. The systematic uncertainties due to the veto cuts in  $K_S^0$  and  $\Xi$  analysis were also studied and found to be small for both particles.

The detector acceptance uniformity for collisions at different primary vertex positions along the beam direction and detector asymmetry between forward and backward halves can also cause systematic uncertainty if they can not be well simulated in embedding data. The  $|z_{vertex}|$  cuts was varied to study the acceptance uniformity, at 39 GeV, the cut was changed within [25, 40] cm. The resulting change in  $p_T$  spectra and hence the systematic errors from this source is negligible. The default rapidity range [-0.5, 0.5] was also divided into the forward half, [0, 0.5], and the backward half, [-0.5, 0]. The max deviations of the resulting  $p_T$  spectra from the default one was accounted for the systematic errors, which is around 3 – 5% at low  $p_T$ .

The final  $p_T$  spectra bin-by-bin systematic error was quadratic sum of all the above sources assuming that there are fully uncorrelated. For  $\Lambda$ , the systematic errors due to feed down corrections were evaluated by propagating the  $\Xi$  systematic errors to  $\Lambda$  raw yield, according to the fractions of those feed down contributions, for simplicity,  $\Xi$  systematic errors were assumed to be uncorrelated with  $\Lambda$ .

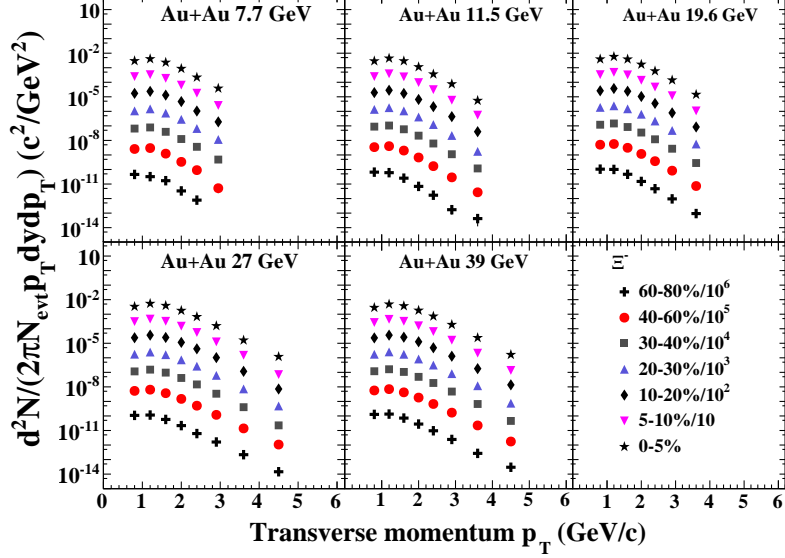


Figure 9: The uncorrected transverse momentum spectra of  $\Xi^-$  at mid-rapidity ( $|y| < 0.5$ ) from Au+Au collisions at different centralities and energies ( $\sqrt{s_{NN}} = 7.7 - 39$  GeV). The data points are scaled by factors of 10 from central to peripheral for clarity.

## 10 Mid-rapidity yields ( $dN/dy$ ) and systematic errors

Due to limited detector acceptance at low  $p_T$  and finite statistics at high  $p_T$ , the spectra were not measured there, hence it needed to be extrapolated in these two regions in order to obtain the  $p_T$  integrated yield ( $dN/dy$ ). The extrapolation at low  $p_T$  is particularly important, since it contributes significantly to both observables, while the extrapolation at unmeasured high  $p_T$  region usually have much smaller contributions.

For  $K_S^0$ , the low  $p_T$  spectra were fitted and hence extrapolated to unmeasured lower  $p_T$  regions with two functions, an exponential function

$$\frac{d^2N}{2\pi p_T dp_T dy} \propto e^{-\frac{m_T}{T}}, \quad (2)$$

and the Levy function

$$\frac{d^2N}{2\pi p_T dp_T dy} \propto \left(1 + \frac{m_T - m}{nT}\right)^{-n}. \quad (3)$$

The intermediate to high  $p_T$  spectra were fitted separately and extrapolated to unmeasured higher  $p_T$  regions with the Levy function and exponential function. The Levy function was used as default for energies above 19.6 GeV, while exponential functions are the default one for energies below 11.5 GeV. The difference between the results from those two functions are considered as part of the systematic errors for  $dN/dy$  and  $\langle m_T \rangle - m_0$ .

For the hyperons,  $\Lambda$  and  $\Xi$ , the default function used for low  $p_T$  extrapolation was a Boltzmann function

$$\frac{d^2N}{2\pi p_T dp_T dy} \propto m_T e^{-\frac{m_T}{T}}. \quad (4)$$

While the high  $p_T$  extrapolation used Levy function for energies above 19.6 GeV, and exponential function for energies below 11.5 GeV. The exponential function was used as the alternative for systematic error estimation.

The integrated  $dN/dy$  was obtained by integrating the  $p_T$  spectra data in the measured  $p_T$  range and the fitted functions in the low  $p_T$  and high  $p_T$  extrapolated ranges. The contribution of high  $p_T$  extrapolation to  $dN/dy$  is almost negligible for all particle species and energies. However, the contribution of low  $p_T$  extrapolation in the integrated  $dN/dy$  are  $\sim 10 - 14\%$  for  $K_S^0$ ,  $\sim 15 - 25\%$  for  $\Lambda$  and  $\bar{\Lambda}$ ,  $\sim 27 - 45\%$  for  $\Xi^-$  and  $\Xi^+$ , and  $\sim 36 - 43\%$  for  $\Omega^-$  and  $\bar{\Omega}^+$ . This contribution are larger for lower energy and more peripheral collisions due to steeper  $p_T$  spectra there.

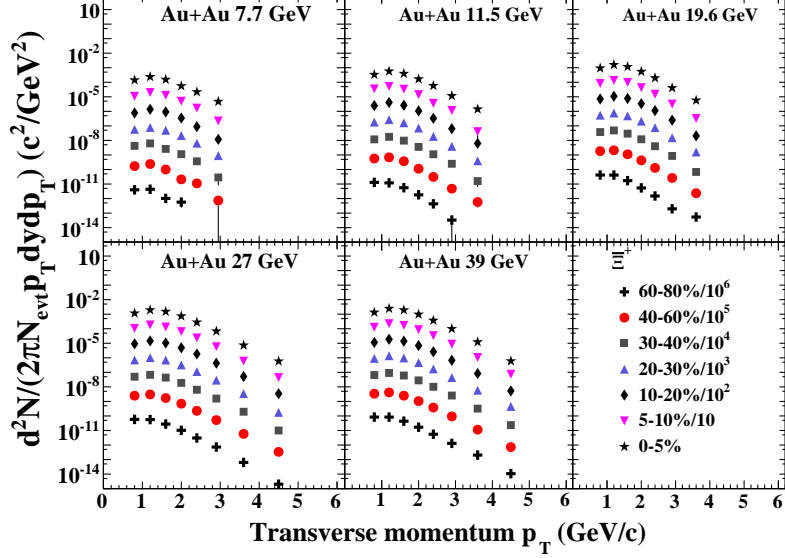


Figure 10: The uncorrected transverse momentum spectra of  $\Xi^+$  at mid-rapidity ( $|y| < 0.5$ ) from Au+Au collisions at different centralities and energies ( $\sqrt{s_{NN}} = 7.7 - 39$  GeV). The data points are scaled by factors of 10 from central to peripheral for clarity.

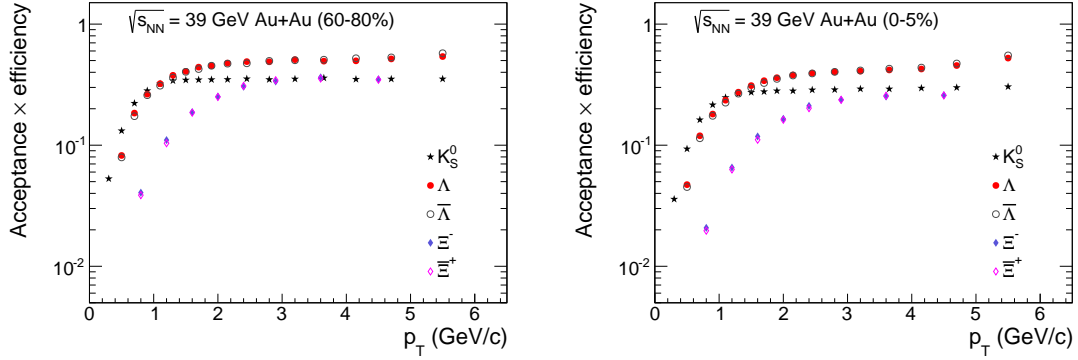


Figure 11: Acceptance and reconstruction efficiency of various strange hadrons at mid-rapidity ( $|y| < 0.5$ ) in peripheral (60-80%, left) and most central (0 – 5%, right) Au+Au collisions at  $\sqrt{s_{NN}} = 39$  GeV. The branching ratios of measured decay channels are not taken into account here.

The systematic error of  $dN/dy$  in the measured  $p_T$  range is simply the sum of the bin-by-bin systematic errors assuming that they are fully correlated. In the extrapolated low  $p_T$  region, the systematic errors were estimated considering two potential sources. Firstly, under different analysis cuts, like the tracking and geometrical cuts, if the resulting corrected  $p_T$  spectra is different, the extrapolation will also be different. This part of extrapolation systematic error is fully correlated with the bin-by-bin systematic errors, hence were added directly to the total  $dN/dy$  systematic errors. Secondly, under the same analysis cut, different extrapolation fitting functions produce different extrapolated yields at low  $p_T$ . This source were studied by changing the fitting functions for the extrapolation, and the resulting systematic errors are assumed to be uncorrelated with the bin-by-bin systematics, and were added quadratically to the total  $dN/dy$  systematic errors. The final systematic errors for  $K_S^0$   $dN/dy$  range from 4% in peripheral collisions at low energies to 7% in most central collisions at 39 GeV in Run10. For  $K_S^0$  in Run11 (19.6 and 27 GeV), it is about 3% for all centralities. For  $\Xi^-$  and  $\Xi^+$ , the values ranges from 8% to 12% in Run10, and about 6% in Run11. For  $\Lambda$  and  $\bar{\Lambda}$ , it ranges from 7 – 9% in Run10, and 4 – 6% in Run11.

Finally, Fig. 20 shows the integrated yield,  $dN/dy$ , per average number of participating nucleon pairs, of various strange hadrons ( $K_S^0$ ,  $\Lambda$ ,  $\bar{\Lambda}$ ,  $\Xi^-$ ,  $\Xi^+$ ) at mid-rapidity ( $|y| < 0.5$ ) as a function of number of participating nucleons,  $N_{part}$ , from Au+Au collisions at  $\sqrt{s_{NN}} = 7.7 - 39$  GeV. The data values can be found in Ref. [13].

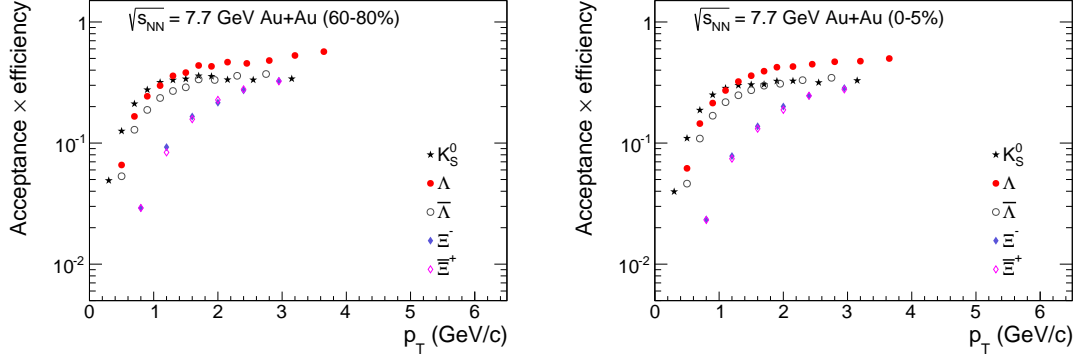


Figure 12: Acceptance and reconstruction efficiency of various strange hadrons at mid-rapidity ( $|y| < 0.5$ ) in peripheral (60-80%, left) and most central (0 – 5%, right) Au+Au collisions at  $\sqrt{s_{NN}} = 7.7$  GeV. The branching ratios of measured decay channels are not taken into account here.

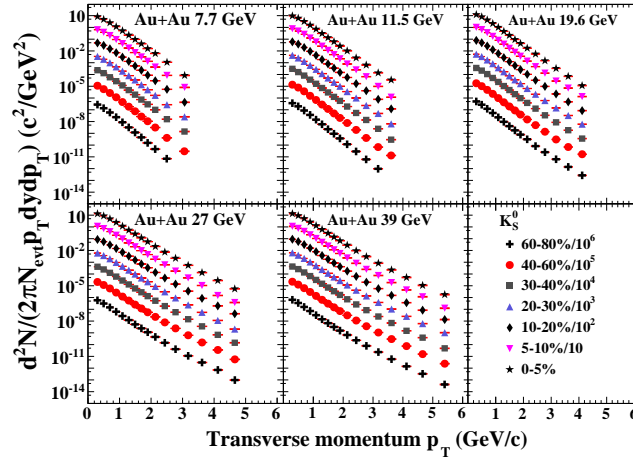


Figure 13: The transverse momentum spectra of  $K_S^0$  at mid-rapidity ( $|y| < 0.5$ ) from Au+Au collisions at different centralities and energies ( $\sqrt{s_{NN}} = 7.7 - 39$  GeV). The data points are scaled by factors of 10 from central to peripheral for clarity. The red vertical shaded bands represent systematic errors.

## References

- [1] L. Adamczyk *et al.* [STAR Collaboration], Phys. Rev. C **88**, 014902 (2013) doi:10.1103/PhysRevC.88.014902 [arXiv:1301.2348 [nucl-ex]].
- [2] Miller M L *et al* 2007 *Ann. Rev. Nucl. Part. Sci.* **57** 205
- [3] <http://www.star.bnl.gov/protected/common/common2010/centrality/>  
<http://www.star.bnl.gov/protected/common/common2011/centrality/>  
[http://www.star.bnl.gov/protected/heavy/aschmah/Presentations/LFS\\_RefMult\\_QA\\_100711\\_V1.pdf](http://www.star.bnl.gov/protected/heavy/aschmah/Presentations/LFS_RefMult_QA_100711_V1.pdf)  
 The ‘StRefMultCorr’ package (ver. 1.8) was checked out from CVS directory ‘offline/users/hmasui/StRefMultCorr’, and packed inside the code of this analysis.
- [4] L. Adamczyk *et al.* [STAR Collaboration], Phys. Rev. C **93**, no. 2, 021903 (2016) doi:10.1103/PhysRevC.93.021903 [arXiv:1506.07605 [nucl-ex]].
- [5] M. Shao, O. Y. Barannikova, X. Dong, Y. Fisyak, L. Ruan, P. Sorensen and Z. Xu, Nucl. Instrum. Meth. A **558**, 419 (2006) doi:10.1016/j.nima.2005.11.251 [nucl-ex/0505026].
- [6] H. Bichsel, Nucl. Instr. and Meth. A **562**, 154 (2006).
- [7] H. Jiang, Ph.D. thesis, UCLA, 2005.

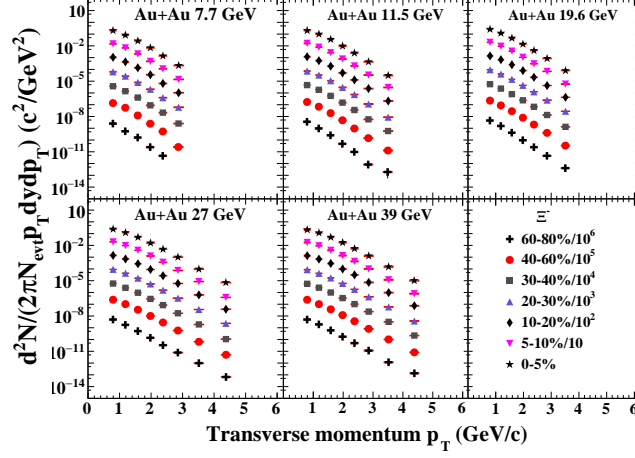


Figure 14: The transverse momentum spectra of  $\Xi^-$  at mid-rapidity ( $|y| < 0.5$ ) from Au+Au collisions at different centralities and energies ( $\sqrt{s_{NN}} = 7.7 - 39$  GeV). The data points are scaled by factors of 10 from central to peripheral for clarity. The red vertical shaded bands represent systematic errors.

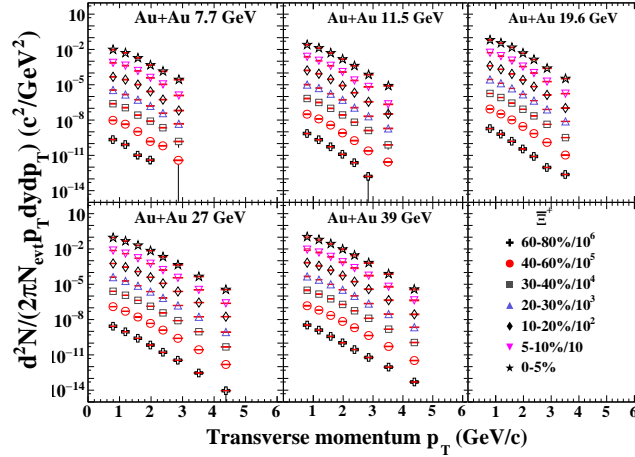


Figure 15: The transverse momentum spectra of  $\Xi^+$  at mid-rapidity ( $|y| < 0.5$ ) from Au+Au collisions at different centralities and energies ( $\sqrt{s_{NN}} = 7.7 - 39$  GeV). The data points are scaled by factors of 10 from central to peripheral for clarity. The red vertical shaded bands represent systematic errors.

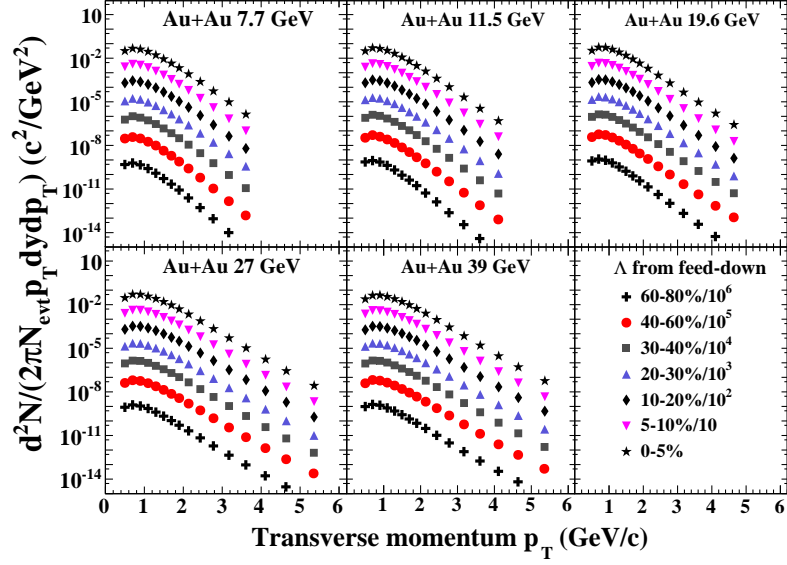


Figure 16: The transverse momentum distribution of  $\Lambda$  from  $\Xi^-$  and  $\Xi^0$  feed-down at mid-rapidity ( $|y| < 0.5$ ) from Au+Au collisions at different centralities and energies ( $\sqrt{s_{NN}} = 7.7 - 39$  GeV). The data points are scaled by factors of 10 from central to peripheral for clarity.

- [8]  $K_S^0$ : <http://www.star.bnl.gov/protected/lfsupc/zhux/beslongpaper/massfitting/ks/>
- [9]  $\Lambda$ : <http://www.star.bnl.gov/protected/lfsupc/zhux/beslongpaper/massfitting/la/>  
 $\bar{\Lambda}$ : <http://www.star.bnl.gov/protected/lfsupc/zhux/beslongpaper/massfitting/ala/>
- [10]  $\Xi^-$ : <http://www.star.bnl.gov/protected/lfsupc/zhux/beslongpaper/massfitting/xi/>  
 $\Xi^+$ : <http://www.star.bnl.gov/protected/lfsupc/zhux/beslongpaper/massfitting/axi/>
- [11] BaseQA: [http://www.star.bnl.gov/protected/embedding/SL10k\\_embed\\_Strangeness\\_AuAu39/](http://www.star.bnl.gov/protected/embedding/SL10k_embed_Strangeness_AuAu39/)  
 $K_S^0$ : <http://www.star.bnl.gov/protected/lfsupc/zhux/beslongpaper/embeddingQA/ks/>  
 $\Lambda$ : <http://www.star.bnl.gov/protected/lfsupc/zhux/beslongpaper/embeddingQA/la/>  
 $\Xi^-$ : <http://www.star.bnl.gov/protected/lfsupc/zhux/beslongpaper/embeddingQA/xi/>
- [12] <http://www.star.bnl.gov/protected/lfsupc/zhux/beslongpaper/efficiency/>
- [13] <http://www.star.bnl.gov/protected/lfspectra/zhux/bes/paper/data/yield/>

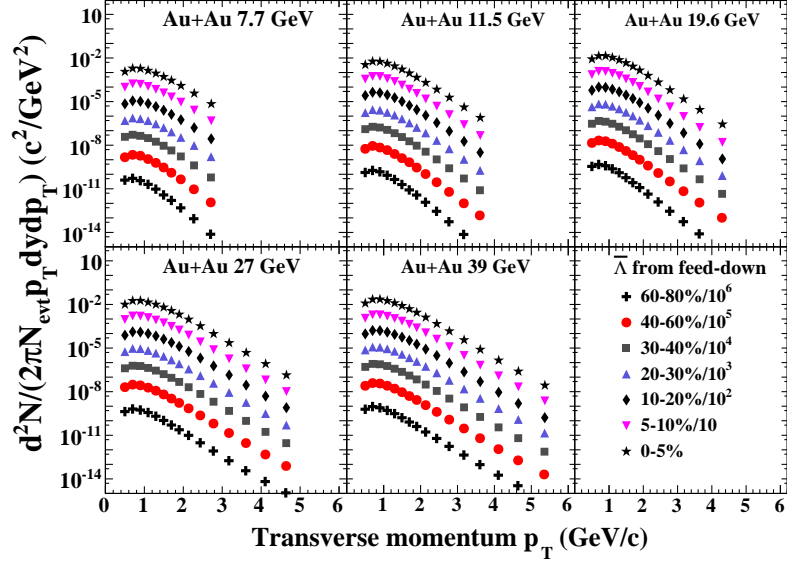


Figure 17: The transverse momentum distribution of  $\bar{\Lambda}$  from  $\Xi^+$  and  $\Xi^0$  feed-down at mid-rapidity ( $|y| < 0.5$ ) from Au+Au collisions at different centralities and energies ( $\sqrt{s_{NN}} = 7.7 - 39$  GeV). The data points are scaled by factors of 10 from central to peripheral for clarity.

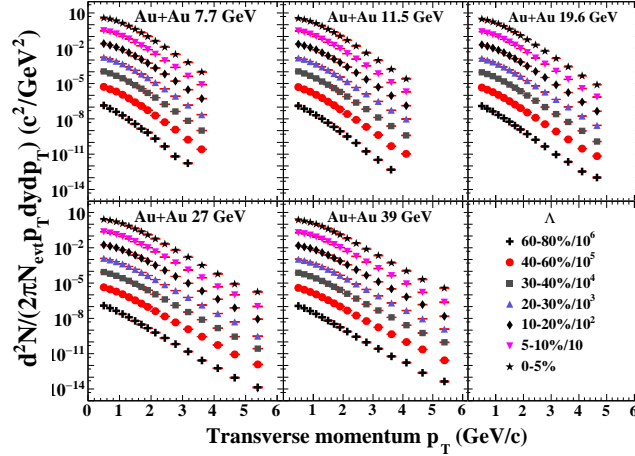


Figure 18: The transverse momentum spectra of  $\Lambda$  at mid-rapidity ( $|y| < 0.5$ ) from Au+Au collisions at different centralities and energies ( $\sqrt{s_{NN}} = 7.7 - 39$  GeV). The spectra are corrected for the feed-down of  $\Xi$  and  $\Xi^0$  decays. The data points are scaled by factors of 10 from central to peripheral for clarity. The red vertical shaded bands represent systematic errors.



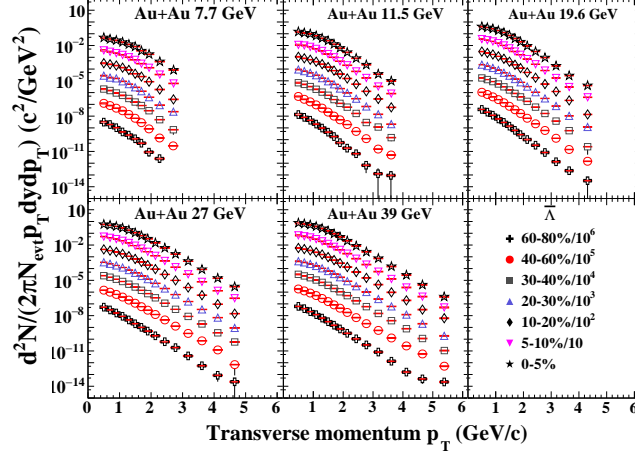


Figure 19: The transverse momentum spectra of  $\bar{\Lambda}$  at mid-rapidity ( $|y| < 0.5$ ) from Au+Au collisions at different centralities and energies ( $\sqrt{s_{\text{NN}}} = 7.7 - 39$  GeV). The spectra are corrected for the feed-down of  $\Xi$  and  $\Xi^0$  decays. The data points are scaled by factors of 10 from central to peripheral for clarity. The red vertical shaded bands represent systematic errors.

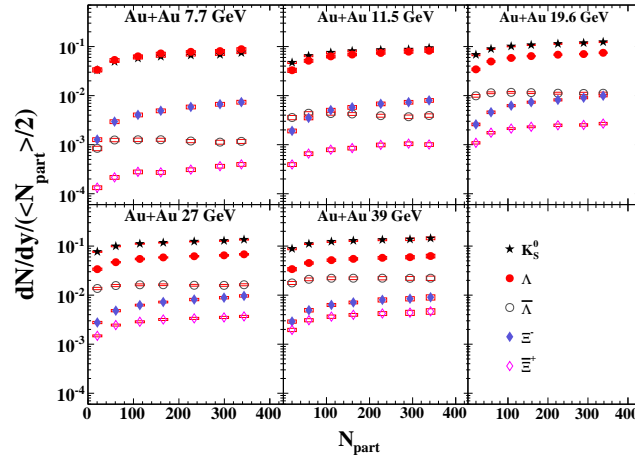


Figure 20: (Color online) The integrated yield,  $dN/dy$ , per average number of participating nucleon pairs, of various strange hadrons ( $K_S^0$ ,  $\Lambda$ ,  $\bar{\Lambda}$ ,  $\Xi^-$ ,  $\Xi^+$ ) at mid-rapidity ( $|y| < 0.5$ ) as a function of number of participating nucleons,  $N_{\text{part}}$ , from Au+Au collisions at  $\sqrt{s_{\text{NN}}} = 7.7 - 39$  GeV. The red boxes denote systematic errors from  $dN/dy$ . Uncertainties in  $N_{\text{part}}$  are not included.